Limit-cycle Oscillations of a pretensed Membrane Strip

Ariel Drachinsky[1] and Daniella E. Raveh[2]

Faculty of Aerospace Engineering, Technion – Israel Institute of Technology

Nomenclature

a	= span length
A	= cross section area
B	= chord length
Ca_{ij}	= aerodynamic modal damping, normalized by the airspeed
C_i	= structural modal damping
C_{mat}	= material damping coefficient
E	= modulus of elasticity
f_i	= frequency of the ith mode
G	= shear modulus
H	= membrane thickness
I	= area moment of inertia
J	= torsional rigidity of the cross section
K_i	= structural stiffness
k	= non-dimensional frequency
Ka_{ij}	= aerodynamic modal stiffness, normalized by the square of the airspeed
L_a	= aerodynamic lift force per unit length
M_a	= aerodynamic pitching moment per unit length
N_0	= initial membrane pre-tension per unit length
Q_a	= aerodynamic pressure on a membrane element
Q_e	= elastic stiffness term
V_0	= airspeed
v_d	= divergence velocity
v_f	= flutter velocity
W	= plunge displacement of a strip
w	= plunge displacement of a membrane element
W_i	= plunge displacement of a strip in the ith mode shape
X_i	= displacement of the ith mode
ΔN	= additional tension due to membrane deflection
$\overline{\varepsilon_x}$	= mid-plane strain averaged over the span
ζ	= damping ratio
θ	= pitch displacement of a strip
θ_i	= pitch displacement of a strip in the ith mode shape
v	= Poisson's ratio
ρ	= membrane density
ρ_a	= air density
σ_0	= pre-stress in the membrane
ω_f	= flutter frequency
ω_i	= frequency of the ith mode

---
[1] MSc Student, Aerospace Engineering Department, Tehcnion – IIT, Haifa 32000.
[2] Associate Professor, Aerospace Engineering Department, Tehcnion – IIT, Haifa 32000.

I.   Abstract

The paper presents a computational and experimental study of the nonlinear aeroelastic response of a pre-tensed, high aspect-ratio, thin membrane strip. The goal of the study is to derive and validate a computational model that can be used for analysis and design of membrane strips, for the purpose of energy harvesting from flutter at low airspeeds. The mathematical model is based on a beam model, accounting for stiffening effects due to pretension and large deformations. The aerodynamic model is a potential flow model. The equations of motion are written as a set of nonlinear ordinary differential equations, using Galerkin's method, and are simulated numerically, and analytically using the Multiple scates method. The nonlinear aeroelastic model is used to study the oscillation characteristics of the membrane strip in the various stability regions. The effects of the initial pretension and non-linear stiffening on the energy-harvesting potential of the system are studied. The combined effect of the preload on the flutter onset speed, on the flutter frequency and amplitude, and on the loss of orbital stability, indicate that an optimal preload can be determined based on the intended airspeed range for energy harvesting. A series of wind tunnel tests is conducted, in which the flutter onset velocity, and the post-flutter frequencies and amplitudes are measured. Good agreement between the experimental data and computational results validate the computational model.

II.   Introduction

In recent years there has been considerable interest in renewable energy resources, and specifically in wind power. One of the devices that were suggested for energy harvesting in low-speed winds is the Windbelt generator, by Shawn Frayne and Jordan McRae with the Humdinger Wind Energy Company [1]. The Windbelt device is a taut, high aspect-ratio membrane that flutters in low-speed winds. Magnets that are attached to the fluttering membrane move in and out of coils, thereby generating electrical power. A somewhat similar device was proposed by Sundararajan et al. [2], where the mechanical vibrations are transformed into electrical power via piezo-electric devices. These devices motivated the current study of the post-flutter characteristics of a high aspect-ratio membrane (i.e., a membrane strip) in low subsonic flows.

Aerodynamics and aeroelastic analyses of 2D membrane wings are well documented in recent literature (e.g. [3–9]). These studies typically refer to membranes that are restrained at the leading and trailing edges, and deal with equilibrium of tension, aerodynamics, and inertial forces on the membrane wing. There is also a vast body of literature on aeroelastic stability and limit-cycle oscillations (LCO) of plates and shells, specifically on plates that are clamped on all sides, or on cantilevered wings (e.g.[10-13]). These studies present different models with different levels of complexity, from a simple beam model, to an arbitrary shell structure modeled with finite elements (FE). The aerodynamic models may vary from linear potential strip theory to full CFD analysis. A recent study, motivated by NASA's mold-line link project for noise reduction of transport aircraft, performed numerical analysis and wind-tunnel testing on membranes of low aspect ratio, in various boundary conditions [12]. None of these studies consider the aeroelastic stability and characteristics of high aspect-ratio membranes, as in the case of the Windbelt device. A somewhat similar, yet different problem studied in the literature is the problem of panel flutter [13-14]. These studies focus on the stability and LCO of thin shells at different aspect ratios, and use similar structural models. However, in the problem of panel flutter, only one side of the panel is exposed to airflow, whereas in the case discussed in the current study both sides of the membrane are subjected to airflow.

The current study presents a nonlinear LCO analysis of a membrane strip, of high aspect ratio, in low subsonic flow. The structural model is nonlinear, employing Galerkin's method on a pre-tensed beam model, accounting for the large deformations during oscillation. The aerodynamic model is a linear potential-flow model. The analysis focuses on the variation of the flutter oscillation amplitude and frequency as a function of airspeed, and the various stability regions. The solution is numerical and with a Parametric study from an energy harvesting point of view is then presented. . The numerical analysis is verified with an analytic multiple scales solution. Wind tunnel tests serve for validating the mathematical model and its assumptions.

III.   Mathematical model

Figure 1 shows the membrane-strip geometry, and the problem setup. The strip dimensions are axbxh (a- span, b-chord, h-thickness), where $a>>b>>h$. The membrane strip is pre-tensed at the short ends (or, clamped at one end and tensioned at the other end), while the long ends, which are the membranes' leading and trailing edges, are free.

As customary in dynamic aeroelastic problems, a modal technique is employed, assuming that the displacements of the membrane-strip can be described by superposition of a few characteristic shapes (typically, structural natural modes). A Galerkin approximation is used, with the first four natural modes as shape functions, in order to obtain a set of nonlinear ordinary differential equations (ODEs) describing the membrane's oscillations due to wind loads. The equations are then integrated numerically using a Runge-Kutta based algorithm.
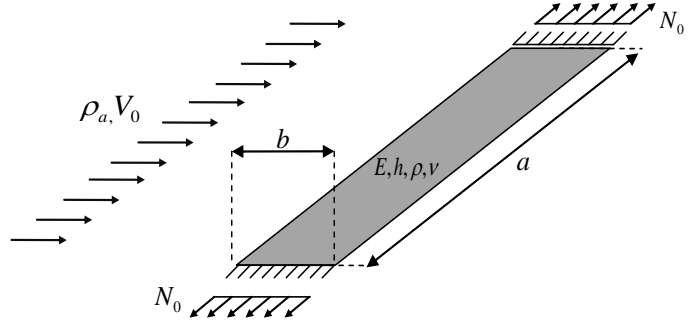
Figure 1: Schematic illustration of the problem.

A. Structural model

The structural model is that of a continuous pre-tensed beam. Due to the high aspect ratio of the membrane we assume that there is no chordwise bending, and therefore each strip (of length dx) of the membrane can move in two degrees of freedom (DOF): plunge (W) and pitch (Θ), as shown in Fig. 2. We verify this assumption in section IVA by comparing modal analysis results computed with this model and with a finite-element model that does include chordwise bending. The mathematical model assumes large displacements, small rotation angles, and small strains. In-plane bending and axial deformations are irrelevant for the analysis and thus are not considered. The equilibrium equation is written for an element dy of the strip (an element dx-dy of the membrane), where the element's displacements can be written in terms of the strip's DOFs as:
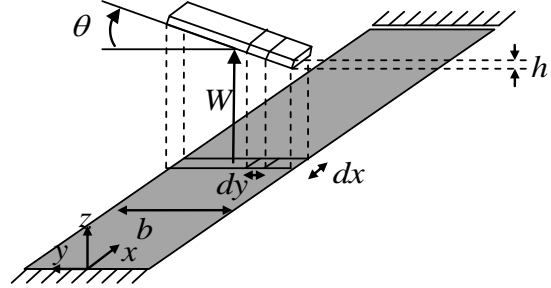

Figure 2: Degrees of freedom of the membrane

$$w(x, y) = W(x) + \theta(x) \cdot y \tag{1}$$

Summing the forces on an element dx-dy yields the membrane's dynamic equation that resembles the string equation:

$$\frac{\partial}{\partial x}\left(N(x, y)\frac{\partial w(x, y)}{\partial x}\right) = \rho h \frac{\partial^2 w(x, y)}{\partial t^2} + Q_a + Q_e \tag{2}$$

where N is the tension in the span direction, per unit length, ρ is the membrane material density, and h is the membrane thickness. Q_a is an aerodynamic pressure term, and Q_e is the elastic term, resulting from bending and torsional rigidity. In Eq. 2 the aerodynamic and elastic terms are considered as external forces. They will be derived later on in this section. The tension in the membrane is provided by:

$$N(x, y) = N_0 + \Delta N \tag{3}$$

Where N_0 is the pre-tension, and ΔN is the additional tension due to the lengthening of the membrane:

$$\Delta N = Eh \cdot \overline{\varepsilon_x}(y) = \frac{Eh}{a} \int_0^a \left(\sqrt{1 + \left(\frac{\partial w}{\partial x} \right)^2} - 1 \right) dx \approx \frac{Eh}{2a} \int_0^a \left(\frac{\partial w(x,y)}{\partial x} \right)^2 dx$$

(4)

where ε_x is the averaged strain (over the thickness) in the span direction. Substituting Eqs. (1), (3), and (4) into Eq. (2), the equilibrium equation, in terms of the strip's DOF, becomes:

$$N_0 \left(\frac{\partial^2 W}{\partial x^2} + y \frac{\partial^2 \theta}{\partial x^2} \right) + \frac{Eh}{2a} \left(\int_0^a \left(\frac{\partial W(x)}{\partial x} + y \frac{\partial \theta(x)}{\partial x} \right)^2 dx \right) \left(\frac{\partial^2 W}{\partial x^2} + y \frac{\partial^2 \theta}{\partial x^2} \right) -$$

$$- \left(\rho h \frac{\partial^2 W}{\partial t^2} + y \frac{\partial^2 \theta}{\partial t^2} \right) - Q_a - Q_e = 0$$

(5)

The elastic terms are formulated for a strip, based on an Euler Bernoulli beam model and Saint Venant's theorem, and are written in terms of the strip's cross-section properties EI and GJ:

$$\int_{-b/2}^{b/2} Q_e \, dy = EI \frac{\partial^4 W}{\partial x^4}, \qquad \int_{-b/2}^{b/2} Q_e \, y \, dy = -GJ \frac{\partial^2 \theta}{\partial x^2}$$

(6)

The aerodynamic terms for the lift and pitching moment on a strip, L_a and M_a respectively, are based on Theodorsen's unsteady aerodynamic model (detailed in the *Aerodynamic model* section):

$$\int_{-b/2}^{b/2} Q_a \, dy \equiv L_a, \qquad \int_{-b/2}^{b/2} Q_a \, y \, dy \equiv M_a$$

(7)

Summing the forces over the chord and requiring overall force and moment equilibrium leads to the force and moment equations for the strip:

$$\rho A \frac{\partial^2 W}{\partial t^2} + L_a - \sigma_0 A \frac{\partial^2 W}{\partial x^2} + EI \frac{\partial^4 W}{\partial x^4} -$$

$$- \frac{E}{2a} \left[\left(A \cdot I_{ww} + I_p \cdot I_{\theta\theta} \right) \frac{\partial^2 W}{\partial x^2} + \left(2 I_p \cdot I_{w\theta} \right) \frac{\partial^2 \theta}{\partial x^2} \right] = 0$$

(8a)

$$\rho I_p \frac{\partial^2 \theta}{\partial t^2} + M_a - \left(\sigma_0 I_p + GJ \right) \frac{\partial^2 \theta}{\partial x^2} -$$

$$- \frac{E}{2a} \left[\left(2 I_p \cdot I_{w\theta} \right) \frac{\partial^2 W}{\partial x^2} + \left(I_p \cdot I_{ww} + A \cdot \frac{b^4}{80} I_{\theta\theta} \right) \frac{\partial^2 \theta}{\partial x^2} \right] = 0$$

(8b)

where:

4

$$I_{ww} \equiv \int_0^a \left(\frac{\partial W}{\partial x}\right)^2 dx, \qquad I_{\theta\theta} \equiv \int_0^a \left(\frac{\partial \theta}{\partial x}\right)^2 dx; \qquad I_{w\theta} \equiv \int_0^a \left(\frac{\partial \theta}{\partial x}\right)\left(\frac{\partial W}{\partial x}\right) dx$$

$$A = bh, \qquad I_p = \frac{hb^3}{12}, \qquad \sigma_0 = \frac{N_0}{h} \tag{9}$$

Provided sufficient pre-tension, the elastic bending stiffness is negligible compared to the membrane stiffness, and the bending stiffness terms are therefore omitted. The elastic torsional stiffness, however, cannot be neglected.

For solution of the non-linear equation we implement Galerkin's method [17], assuming that the nonlinear solution can be described by a linear combination of shape functions:

$$W(x,t) \approx X_1(t)W_1(x) + X_2(t)W_2(x) + X_3(t)W_3(x) + X_4(t)W_4(x)$$
$$\theta(x,t) \approx X_1(t)\theta_1(x) + X_2(t)\theta_2(x) + X_3(t)\theta_3(x) + X_4(t)\theta_4(x) \tag{10}$$

where W_i and θ_i are the plunge and pitch displacements in the ith shape function respectively, and X_i are the generalized displacements. The shape functions are the structural, natural mode shapes presented in appendix A, obtained from eigensolution of the linearized homogeneous equations:

$$\sigma_0 A \frac{\partial^2 W}{\partial x^2} - \rho A \frac{\partial^2 W}{\partial t^2} = 0 \tag{11a}$$

$$(\sigma_0 I_p + GJ) \frac{\partial^2 \theta}{\partial x^2} - \rho I_p \frac{\partial^2 \theta}{\partial t^2} = 0 \tag{11b}$$

Note that in each mode either θ_i or W_i is zero due to the structural uncoupling of the bending and torsion. Implementing Galerkin's method on the element's equilibrium equation (Eq. (2)) leads to:

$$\int_0^a \int_{-b/2}^{b/2} \left[\frac{\partial}{\partial x}\left(N(x,y)\frac{\partial w(x,y)}{\partial x}\right) - \rho h \frac{\partial^2 w(x,y)}{\partial t^2} - Q_a - Q_e\right] \cdot w_i \, dy dx = 0 \tag{12}$$

where w_i is the element's displacement in the ith mode. Substituting Eq. (1) yields:

$$\int_0^a \int_{-b/2}^{b/2} [r] dy \cdot W_i(x) dx + \int_0^a \int_{-b/2}^{b/2} [r] \cdot y dy \cdot \theta_i(x) dx = 0 \tag{13}$$

where

$$r \equiv \left[\frac{\partial}{\partial x}\left(N(x,y)\frac{\partial w(x,y)}{\partial x}\right) - \rho h \frac{\partial^2 w(x,y)}{\partial t^2} - Q_a - Q_e\right] \tag{14}$$

Integrating on dy yields:

$$\int_0^a (r_1)W_i dx + \int_0^a (r_2)\theta_i dx = 0$$

(15)

where r_1 and r_2 are the left-hand side terms of Eq. (8a) and (8b) respectively. Integrating on dx, four differential equations are obtained:

$$\ddot{X}_1 + K_1 X_1 + \xi_{11} X_1^3 + \xi_{12} X_1 X_2^2 + \xi_{13} X_1 X_3^2 + \xi_{14} X_1 X_4^2 + \xi_{234} X_2 X_3 X_4 +$$
$$+ \frac{2}{A\rho a} \int_0^a L_a \cdot u_1 dx + \frac{2}{A\rho a} \int_0^a M_a \cdot u_1 dx = 0$$

(17a)

$$\ddot{X}_2 + K_2 X_2 + \xi_{21} X_2 X_1^2 + \xi_{22} X_2^3 + \xi_{23} X_2 X_3^2 + \xi_{24} X_4 X_4^2 + \xi_{134} X_1 X_3 X_4 +$$
$$+ \frac{2}{I_p \rho a} \int_0^a L_a \cdot u_2 dx + \frac{2}{I_p \rho a} \int_0^a M_a \cdot u_2 dx = 0$$

(17b)

$$\ddot{X}_3 + K_3 X_3 + \xi_{31} X_3 X_1^2 + \xi_{32} X_3 X_2^2 + \xi_{33} X_3^3 + \xi_{34} X_3 X_4^2 + \xi_{124} X_1 X_2 X_4 +$$
$$+ \frac{2}{A\rho a} \int_0^a L_a \cdot u_3 dx + \frac{2}{\rho a} \int_0^a M_a \cdot u_3 dx = 0$$

(17c)

$$\ddot{X}_4 + K_4 X_4 + \xi_{41} X_4 X_1^2 + \xi_{42} X_4 X_2^2 + \xi_{43} X_4 X_3^2 + \xi_{44} X_4^3 + \xi_{123} X_1 X_2 X_3 +$$
$$+ \frac{2}{I_p \rho a} \int_0^a L_a \cdot u_4 dx + \frac{2}{I_p \rho a} \int_0^a M_a \cdot u_4 dx = 0$$

(17d)

where the K and ξ terms are defined in appendix A.

Structural, viscous damping can be added in several ways. One approach is to assume a linear relation between the displacement rate and the force:

$$C_i = \int_0^a \int_{-b/2}^{b/2} \left[C_{mat} \frac{\partial w}{\partial t} \right] \cdot w_i dy dx$$

(18a)

and adding Eq. (18a) to Eq. (12). Another approach is to assume a linear relation between the strain rate and the damping force, thus between the rate of curvature change and the resultant force

$$C_i = \int_0^a \int_{-b/2}^{b/2} \left[C_{mat} \frac{\partial^3 w}{\partial x^2 \partial t} \right] \cdot w_i dy dx$$

(18b)

and adding Eq. (18b) to Eq. (12). Note that C_{mat} has different dimensions in Eqs. (18a) and (18b). Since the coefficients C_{mat} are difficult to establish, it is customary to assume a modal damping coefficient, ζ_i, based on experience or vibration test:

$$C_i = 2\zeta_i \omega_i \tag{18c}$$

In the following analyses we assume no structural damping, $\zeta_i = C_{mat} = 0$.

B. Aerodynamic model

The aerodynamic lift and moment, per unit length, are based on Theodorsen's strip theory, assuming potential flow, a flat, rigid, and thin section that oscillates in two degrees of freedom of pitch and plunge, in a constant frequency, with no aerodynamic interaction between sections. The aerodynamic force in each DOF consists of two terms: one due to modal displacement and one due to modal velocity.

$$\int_0^a L_a\left(W,\dot{W},\theta,\dot{\theta}\right)\cdot W_i \cdot dx + \int_0^a M_a\left(W,\dot{W},\theta,\dot{\theta}\right)\cdot \theta_i \cdot dx =$$
$$= FX_i\left(W,\theta\right) + F\dot{X}_i\left(\dot{W},\dot{\theta}\right) \tag{19}$$

Substitution of the oscillatory derivatives found in [18] and integration yields:

$$FX_1 = -\rho_a V_0^2 \frac{a}{2} L_z(k) X_1 + \rho_a V_0^2 \frac{a}{2} L_\theta(k) X_2$$

$$FX_2 = -\rho_a V_0^2 b \frac{a}{2} M_z(k) X_1 + \rho_a V_0^2 b \frac{a}{2} M_\theta(k) X_2$$

$$FX_3 = -\rho_a V_0^2 \frac{a}{2} L_z(k) X_3 + \rho_a V_0^2 \frac{a}{2} L_\theta(k) X_4 \tag{20a}$$

$$FX_4 = -\rho_a V_0^2 b \frac{a}{2} M_z(k) X_3 + \rho_a V_0^2 b \frac{a}{2} M_\theta(k) X_4$$

$$F\dot{X}_1 = -\rho_a V_0 \frac{ab}{4} L_{\dot{z}}(k) \dot{X}_1 + \rho_a V_0 \frac{ab}{4} L_{\dot{\theta}}(k) \dot{X}_2$$

$$F\dot{X}_2 = -\rho_a V_0 \frac{ab^2}{4} M_{\dot{z}}(k) \dot{X}_1 + \rho_a V_0 \frac{ab^2}{4} M_{\dot{\theta}}(k) \dot{X}_2$$

$$F\dot{X}_3 = -\rho_a V_0 \frac{ab}{4} L_{\dot{z}}(k) \dot{X}_3 + \rho_a V_0 \frac{ab}{4} L_{\dot{\theta}}(k) \dot{X}_4 \tag{20b}$$

$$F\dot{X}_4 = -\rho_a V_0 \frac{ab^2}{4} M_{\dot{z}}(k) \dot{X}_3 + \rho_a V_0 \frac{ab^2}{4} M_{\dot{\theta}}(k) \dot{X}_4$$

where k is the non-dimensional frequency, defined as:

$$k = \frac{\omega b}{2v} \tag{21}$$

After normalization of the generalized aerodynamic forces, similarly to the structural terms, and addition of the damping terms, Eq. (22) is obtained. The coefficients are provided in appendix A. Note that there is no linear coupling between DOFs 1,2 and DOFs 3,4, neither in the structural nor in the aerodynamic terms.

$$
\ddot{X}_1 + \left(C_1 - vC_{a11}\right)\dot{X}_1 - vC_{a12}\dot{X}_2 + \left(K_1 - v^2 K_{a11}\right)X_1 - v^2 K_{a12}X_2 +
$$
$$
+\xi_{11}X_1^3 + \xi_{12}X_1X_2^2 + \xi_{13}X_1X_3^2 + \xi_{14}X_1X_4^2 + \xi_{234}X_2X_3X_4 = 0
$$

(22a)

$$
\ddot{X}_2 + \left(C_2 - vC_{a22}\right)\dot{X}_2 - vC_{a21}\dot{X}_1 + \left(K_2 - v^2 K_{a22}\right)X_2 - v^2 K_{a21}X_2 +
$$
$$
+\xi_{21}X_2X_1^2 + \xi_{22}X_2^3 + \xi_{23}X_2X_3^2 + \xi_{24}X_4X_4^2 + \xi_{134}X_1X_3X_4 = 0
$$

(22b)

$$
\ddot{X}_3 + \left(C_3 - vC_{a33}\right)\dot{X}_3 - vC_{a34}\dot{X}_4 + \left(K_3 - v^2 K_{a33}\right)X_3 - v^2 K_{a34}X_4 +
$$
$$
+\xi_{31}X_3X_1^2 + \xi_{32}X_3X_2^2 + \xi_{33}X_3^3 + \xi_{34}X_3X_4^2 + \xi_{124}X_1X_2X_4 = 0
$$

(22c)

$$
\ddot{X}_4 + \left(C_4 - vC_{a44}\right)\dot{X}_3 - vC_{a43}\dot{X}_3 + \left(K_4 - v^2 K_{a44}\right)X_4 - v^2 K_{a43}X_3 +
$$
$$
+\xi_{41}X_4X_1^2 + \xi_{42}X_4X_2^2 + \xi_{43}X_4X_3^2 + \xi_{44}X_4^3 + \xi_{123}X_1X_2X_3 = 0
$$

(22d)

C. Solution of the aeroelastic equations

Equation 22 is solved numerically using Matlab's ODE45 solver, which is an adaptive solver that integrates a system of ODEs using a 4th order Runge-Kutta formula (with a 5th order correction). Since the aerodynamic terms are functions of the oscillation frequency, the solution is followed by spectral analysis. After obtaining the oscillation frequency, the aerodynamic terms are updated, and the problem is simulated again. This procedure is repeated until convergence.

D. Power calculation

After solution of the aeroelastic equation, a calculation of the work done by the aerodynamic forces can be made. Integrating the work over an oscillation cycle yields the average power generated by the external forces (aerodynamics). The calculation is made in modal coordinates:

$$
W = \frac{1}{T}\sum_{i=1}^{4}\int_{t}^{t+T}\left(FX_i\left(X_1,X_2,X_3,X_4\right)\cdot\dot{X}_i + F\dot{X}_i\left(\dot{X}_1,\dot{X}_2,\dot{X}_3,\dot{X}_4\right)\cdot\dot{X}_i\right)d\tau
$$

(23)

where FX_i and $F\dot{X}_i$ are the aerodynamic forces presented in Eq. 20. This estimate serves as an upper boundary for the energy that can be harvested, since the energy of the system would generally be the input energy times an efficiency factor.

It is noted that the integration in Eq. (23) is performed only on the external forces (only on the aerodynamic terms). The total work of the system (including the structural terms as well as the aerodynamic terms) equals zero. Since the system is above flutter speed, the aerodynamic damping is negative, leading to constant power flow into the system. Energy flows out of the system through the nonlinear terms and the structural damping. Attachment of an energy harvesting system would affect the solution, causing it to oscillate in smaller amplitudes. This is why the power calculation in Eq. (23) yields an upper boundary value.

E. Strain calculation

The analysis is validated with an experiment presented in section VI. The main measurement in the experiment is the strain in the longtitutional direction, on a pre-selected point on the membrane. Hence, in order to get a better basis for comparison with the experimental data, the strain in the membrane is evaluated numerically. The strain in the membrane is the result of three components:

$$\varepsilon = \varepsilon_0 + \varepsilon_b + \varepsilon_T \tag{24}$$

The first component is strain due to pre-tension:

$$\varepsilon_0 = \frac{N_0}{EA} \tag{25}$$

The second component is the strain due to the bending of the membrane:

$$\varepsilon_b = \frac{\sigma}{E} = \frac{Mh}{2EI} = \frac{\partial^2 w}{\partial x^2}\frac{h}{2} \tag{26}$$

and according to Eqs. (1) and (10)

$$\frac{\partial^2 w}{\partial x^2}(x,t) \approx \sum_{i=1}^{4} X_i \left(\frac{\partial^2 W_i}{\partial x^2} + y\frac{\partial^2 \theta_i}{\partial x^2} \right) \tag{27}$$

Note that though the bending contribution to the stiffness was negligible, the strain due to bending is not.
The third component results from the additional tension in the membrane, due to the large deformation (ΔN):

$$\varepsilon_T = \frac{\Delta N}{Eh} = \frac{1}{2a}\int_0^a \left(\frac{\partial w(x,y)}{\partial x} \right)^2 dx = \frac{X_i^2}{2a}\int_0^a \left(\sum_{i=1}^{4}\left(\frac{\partial W_i}{\partial x} + y\frac{\partial \theta_i}{\partial x} \right) \right)^2 dx \tag{28}$$

Note that while the first component is static, the second is dependent on X(t) and therefore oscillates in the LCO frequency. The third component is dependent on $X(t)^2$ and therefore oscillates in a frequency that is double the LCO frequency, and not about zero:

$$X \approx X_0 \cos(\omega t) \rightarrow X^2 \approx \frac{X_0}{2}\left(1 + \cos(2\omega t)\right) \tag{29}$$

IV. Numerical test case

The membrane in the test case is made of Mylar, with the geometrical parameters and properties detailed in table 1.

Table 1: Structural parameters.

Property	a	b	h	σ_0	E	ρ	ζ	ρ_a	v
value	596	25	0.25	3.89	6980	1430	0.0	1.225	0.39
units	mm	mm	mm	MPa	MPa	Kg/m^3	%	Kg/m^3	--

9

A. Linear analysis

Modal analysis and linear flutter analysis were conducted for the membrane in three different ways as follows:
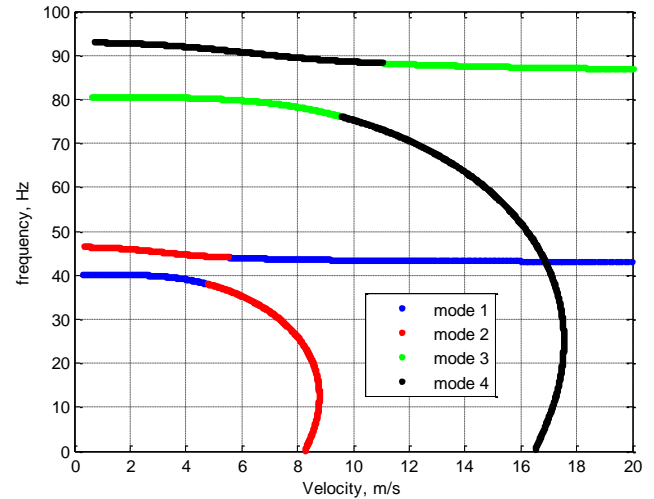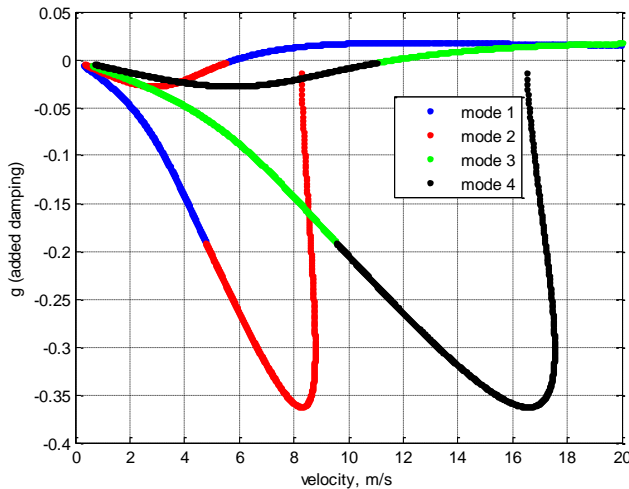
1. Modal analysis using the continuous pre-tensed beam model derived above. Since flutter analysis is linear, linearization was made about zero deflections. A k-method flutter analysis [18] was performed using the resulting four-mode system, with strip-method aerodynamics.
2. Modal analysis in Nastran using shell elements. The resulting 10 modes were used in Zaero g-method flutter analysis with unsteady panel aerodynamics (Zona 6)[19].
3. Modal analysis for a FE beam model, augmented with the geometric stiffness matrix (due to pretension), in a Matlab code. The resulting 10 modes were used in a k-method flutter analysis, with strip theory aerodynamics.

The objective of *analysis 2* was to verify the assumption that there is no chordwise bending in the first modes, and thus that the beam model is appropriate. In addition, it provided comparison between strip and panel aerodynamic models. The objective of analysis 3was to support the exclusion of the bending stiffness terms from the continuous pre-tensed beam model, and verify that four modes are sufficient for flutter analysis. A comparison between the results of the three analyses is presented in Table 2, showing good agreement. The first bending frequency computed by model 1 (without the bending stiffness), is slightly lowered (by 1.1%), which leads to a 3% reduction in flutter speed.

Figure 3 shows the V-g plot of the continuous pre-tensed-beam model. Flutter occurs at 6.2 m/s for the first bending and first torsion modes, and divergence, of the torsion mode, at 8.6 m/s. Similar plots were obtained with the other two models.

Table 2: Modal and flutter analysis comparison between different models.

	four modes continuous pre-tensed-beam	10 modes shell+panel model	10 modes FE beam+strip model
1st Bending [Hz]	43.9	44.2	44.4
1st Torsion [Hz]	49.1	48.7	49.2
2nd Bending [Hz]	87.9	88.4	88.8
2nd Torsion [Hz]	98.2	98.3	98.5
V_f [m/s]	6.2	6.4	6.4
V_d [m/s]	8.6	8.9	8.6

B. Nonlinear analysis

Equation 22 was simulated at velocities up to five times the flutter velocity. In order to assess the sensitivity of the problem to initial conditions (IC) the response in each airspeed was simulated twice, with two sets of IC, of large and small

displacements, where a large displacement is an order of magnitude larger than the computed membrane's vibration amplitude, and a small displacement is an order of magnitude lower. Figure 4 shows a plot of the maximum displacement of the mid-span leading edge (LE) point at steady oscillations versus the ratio of airspeed to flutter speed (where flutter speed is the linearly computed flutter speed). At the high velocities, the oscillation is chaotic and no steady state is achieved. The values plotted at these velocities are the maximum values of the last 100 out of 3000 periods.
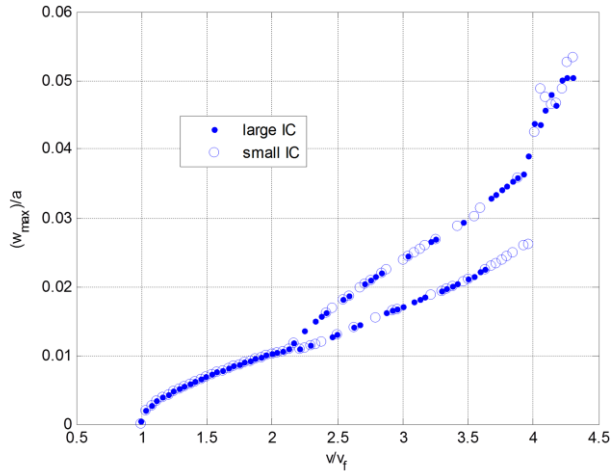
Figure 4: LE maximum displacement vs. airspeed
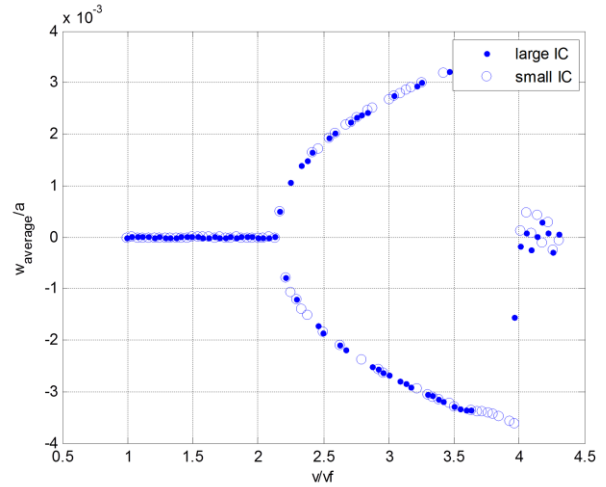
Figure 5: LE average displacement vs. airspeed

Figure 5 shows the average displacement (over time) of the mid-span leading edge point at steady oscillations. Three stability thresholds are seen in Figs. (4) and (5), dividing the membrane oscillations into four regions, as a function of airspeed, as described in table 3.

Table 3: Different stability regions.

region	v/vf	
1	0-1	Stable. All oscillations decay.
2	1-2.2	LCO 1st and 2nd modes.
3	2.2-3.7	LCO 1st and 2nd modes with a static offset (the oscillation is about non-zero deflection). The onset of this phenomenon does not occur at the linearly computed divergence speed.
4	>3.7	Gradual loss of periodicity, turning into chaotic oscillations.

Figure 6 shows the modal displacements as a function of airspeed (where the modal bending deformations are normalized by span length, and the torsion deformations by span-over-half-chord). It is seen that the third and fourth modes remain stable (oscillations decay). This is unlike in the linear stability analysis where there is also flutter of the third and fourth modes. This is due to the stiffening, resulting from large deformations of the first and second modes.

Figure 7 shows the membrane's mid-span leading edge oscillations in each of the four regions. While in region 2 the oscillations are about zero-displacement, in region 3 there is a static offset displacement. It is due to this static offset that the maximum displacement in Fig. 4 appears to depend on the IC. If this static offset is subtracted from the solution, both branches coincide.
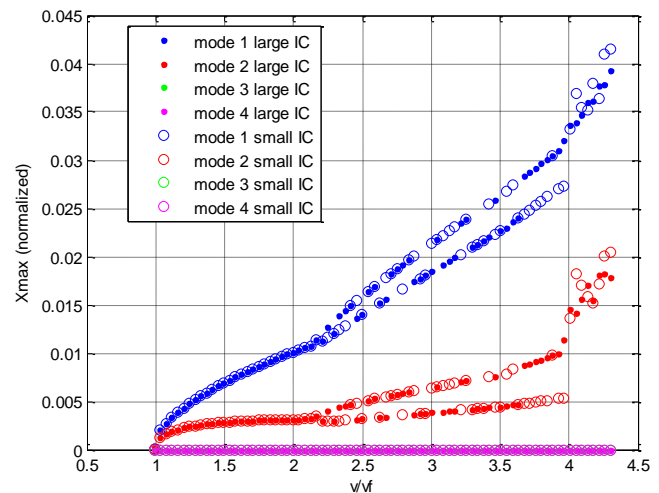

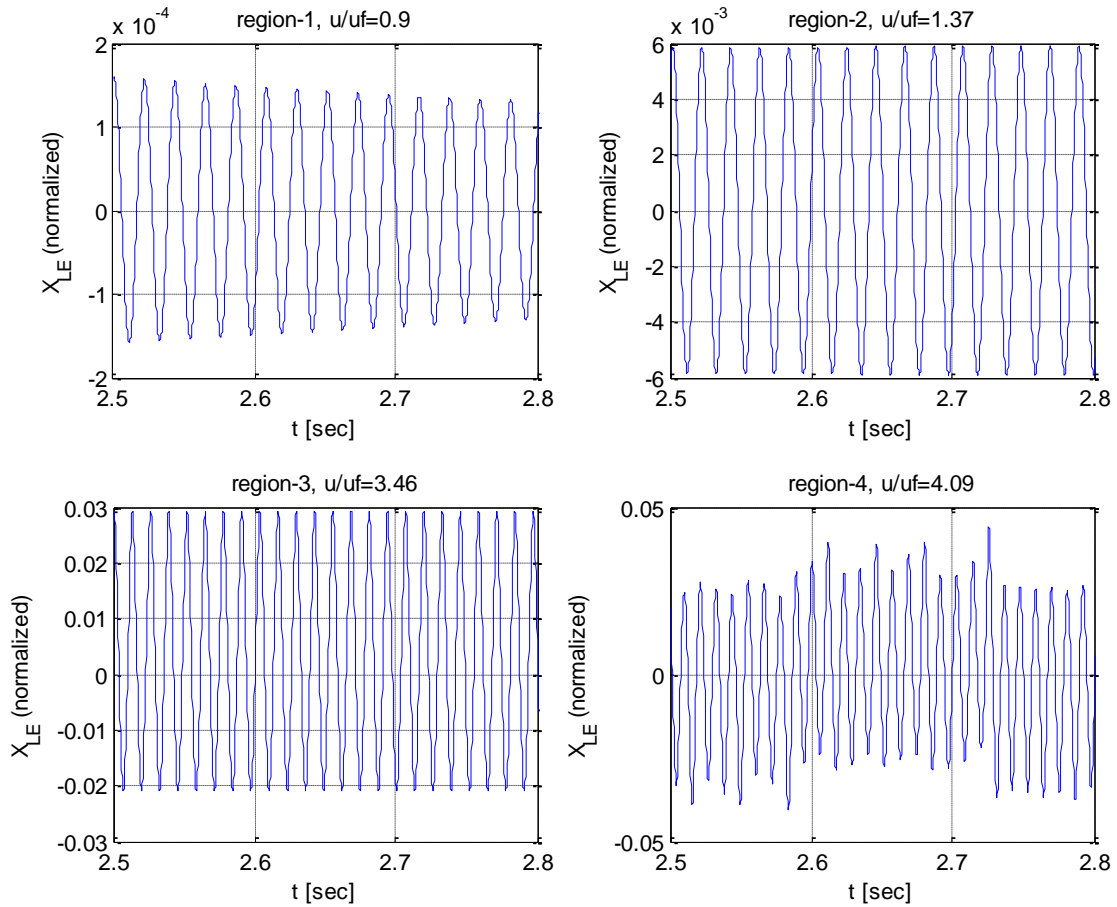Figure 6: Modal amplitude vs. airspeed

Figure 7: Sample time history plots at the different stability regions

Spectral analysis was conducted at each speed, using the FFT algorithm. Figure 8 shows the variation of the dominant frequency as a function of airspeed. It is seen that the frequency increases bi-linearly with the airspeed, independent of the IC. The increase in frequency results from aerodynamic stiffness, and also from the nonlinear elastic term, which is governed by the cube of the displacement magnitude. The change in frequency growth rate seen at 2.2 times flutter speed corresponds to the static offset in membrane oscillations. It is likely due to the larger deformations and, as a result, the additional stiffness.

Sample results of the spectral analysis from each of the stability regions are shown in Fig. 9. Though the oscillation is non-harmonic, a dominant frequency appears in all cases, for both modes. In regions one and two, the oscillation is very close to harmonic, and only one frequency is observed. Note that in region one, the amplitude is very small. This is due to the decay of the oscillations in this region. Region two is characterized by a classical LCO. In region three, a large peak appears at zero frequency due to the static offset of the vibration. In addition, a content of higher harmonics can be seen, especially in the torsion (second) mode. In region four, there is a dominant frequency, plusa small frequency content in a large spectrum.
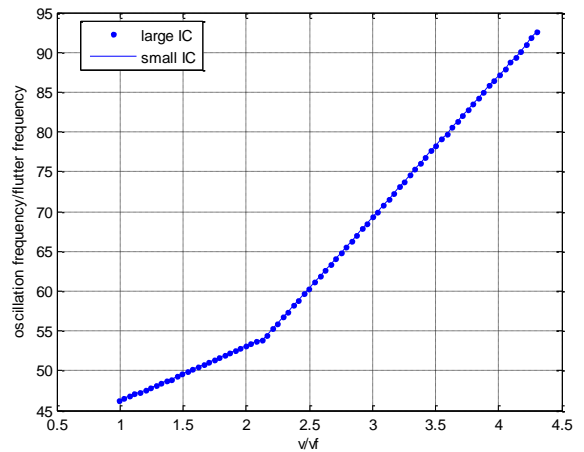

Figure 8: oscillation frequency vs. airspeed

12

We recall that the aerodynamic model assumes vibration in a single frequency. The oscillations in regions three and four do not adhere to this assumption, thus the results there are phenomenological and not necessarily accurate.
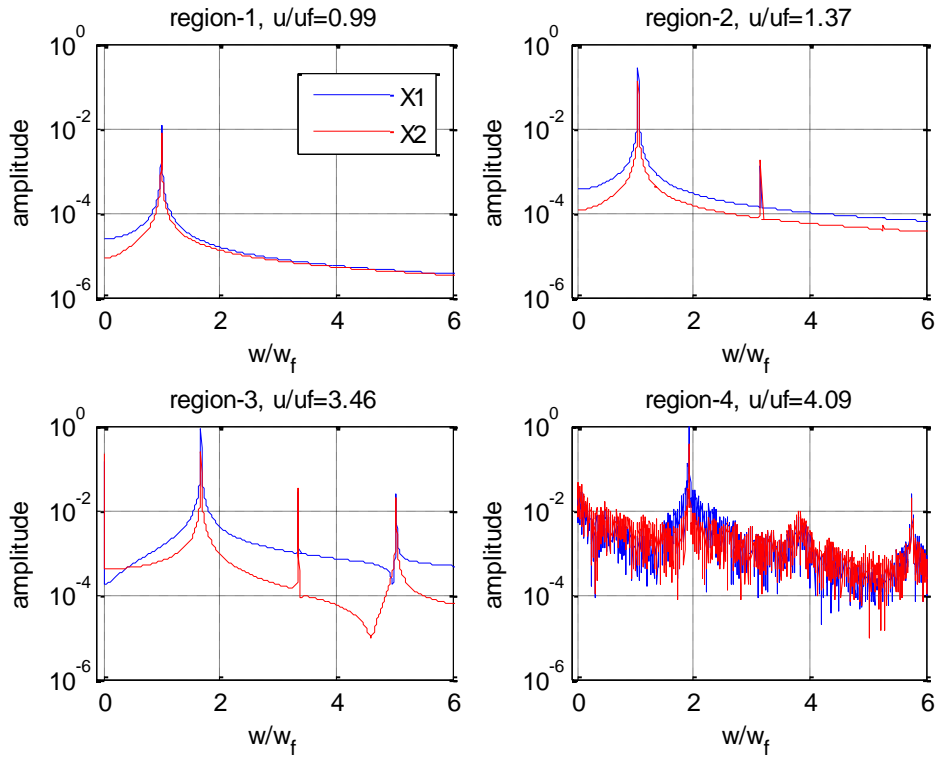

Figure 9: Frequency content at different stability regions

Figure 10 shows a time history of each of the strain components discussed in III, E. , and the total strain, at a sample airspeed. It shows that although the bending term is negligible in the stiffness calculation, it effects the measured strain.
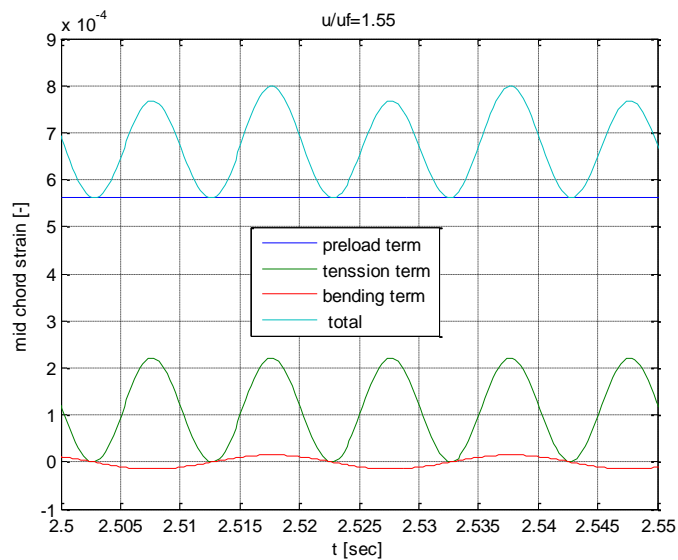
Figure 10: Strain time history

13

V. Multiple scales solution

The multiple scales solution was conducted on a reduced, two-mode, system. The system is written in a non-dimensional matrix form (Eq. (23)). The scaling parameters are defined in Eq. (24) and the matrix and vector terms are defined in Eq. 25.

$$\{Z\}_{\tau\tau} - v[C_a]\{Z\}_\tau + \left([K_s] - v^2[K_a]\right)\{Z\} + \{f\} = 0 \tag{23}$$

$$\{Z\} \equiv \frac{1}{a}\begin{Bmatrix} X_1 \\ X_2 \cdot b \end{Bmatrix}, \qquad \tau \equiv \omega_1 t \tag{24}$$

$$[C_a] = \frac{1}{\omega_1}\begin{bmatrix} C_{a11} & C_{a12}/b \\ bC_{a21} & C_{a22} \end{bmatrix}, \qquad [K_a] = \frac{1}{\omega_1^2}\begin{bmatrix} K_{a11} & K_{a12}/b \\ bK_{a21} & K_{a22} \end{bmatrix} \tag{a25}$$

$$[K_s] = \frac{1}{\omega_1^2}\begin{bmatrix} K_1 & 0 \\ 0 & K_2 \end{bmatrix}, \qquad \{f\} = \begin{Bmatrix} \xi_{11}Z_1^3 + \xi_{12}Z_1Z_2^2 \\ \xi_{22}Z_2^3 + \xi_{21}Z_2Z_1^2 \end{Bmatrix} \tag{b25}$$

The following assumptions are made and substituted into Eq. (23): small displacements (Eq. (26)):, multiple time scale(Eq. (27)), large cubic coupling (Eq. (28)), and a small detuning from the flutter velocity (Eq. (29)),

$$\{Z\} = \varepsilon\{Z_1\} + \varepsilon^2\{Z_2\}\ldots \tag{26}$$

$$T_n = \varepsilon^n\tau; \qquad n = 0,1,\ldots \tag{27}$$

$$\xi_{ij} = \frac{\xi_{ij}}{\varepsilon} \tag{28}$$

$$v = v_f + \varepsilon v_\delta \tag{29}$$

where, ε is a small parameter. Collecting terms of equal order of ε yields:

$$0(\varepsilon): \qquad D_0^2\{Z_1\}_{\tau\tau} - vD_0[C_a]\{Z_1\}_\tau + \left([K_s] - v_f^2[K_a]\right)\{Z_1\} = 0 \tag{30}$$

$$0(\varepsilon^2): \quad \begin{aligned} D_0^2\{Z_2\}_{\tau\tau} - vD_0[C_a]\{Z_2\}_{\tau\tau} + \left([K_s] - v_f^2[K_a]\right)\{Z_2\} = \\ = -2D_0D_1\{X_1\} + v_fD_1[C_a]\{X_1\} + v_\delta D_0[C_a]\{X_1\} + \\ +2v_f v_\delta[K_a]\{X_1\} + \{f(X_1)\} \end{aligned} \tag{31}$$

The general solution of the first order equation (Eq. (30)) is:

$$\{Z_1\} = \sum_m c_m(T_1)\{V_m\}e^{\lambda_m T_0} \tag{32}$$

where: λ_m are complex eigen values of the equation, $\{V_m\}$ are the eigen vectors, $c_m(T_1)$ are complex, time dependent, functions describing the amplitudes of the frequency response. All of the obtained modes except the flutter mode (recognized by the flutter frequency) decay with time. Therefore, leaving only the non-decaying solution yields:

$$\{Z_1\} = c_f(T_1)\{V_f\}e^{i\omega_f T_0} + cc \tag{33}$$

Note that the flutter frequency, in this section is non-dimensional. Substituting Eq. (33) into Eq. (31) yield:

$$D_0^2\{Z_2\} - vD_0[C_a]\{Z_2\} + ([K_s] - v_f^2[K_a])\{Z_2\} =$$

$$= \begin{pmatrix} (-2i\omega_f[I] - v_f[C_a])\{V_f\}(D_1c_f) + \\ +(i\omega_f[C_a] + 2v_f[K_a])\{V_f\}v_\delta c_f + \\ +\{f(V_f)\}|c_f|^2 c_f \end{pmatrix} e^{i\omega_f T_0} + cc + ... \tag{34}$$

where:

$$\{f(V_f)\} = \begin{Bmatrix} 3\xi_{11}|V_1|^2 V_1 + \xi_{12}(V_2^2\overline{V_1} + 2|V_2|^2 V_2) \\ 3\xi_{22}|V_2|^2 V_2 + \xi_{21}(V_1^2\overline{V_2} + 2|V_1|^2 V_1) \end{Bmatrix}; \qquad V_f = \begin{Bmatrix} V_1 \\ V_2 \end{Bmatrix} \tag{35}$$

Demanding elimination of the secular terms in Eq. (34) leads:

$$\{U_f\}^T \begin{pmatrix} (-2i\omega_f[I] - v_f[C_a])\{V_f\}(D_1c_f) + \\ +(i\omega_f[C_a] + 2v_f[K_a])\{V_f\}v_\delta c_f + \\ +\{f(V_f)\}|c_f|^2 c_f \end{pmatrix} = 0 \tag{36}$$

where Uf is the left eigenvector of equation 6.5a that corresponds to the flutter frequency. Assuming a polar solution (Eq. (37)) and separation of the equation to real and imaginary equations leads to Eq. (38).

$$c_f = \frac{1}{2}P(T_2)e^{iQ(T_2)} \tag{37}$$

$$\begin{cases} D_1 P = P(M_1 v_\delta + M_2 P^2) \\ D_1 Q = N_1 U_\delta + N_2 P^2 \end{cases} \tag{38}$$

where:

$$M_1 = \mathrm{Re}\left(\frac{\{U_f^T\}(i\omega_f[C_a] + 2v_f[K_a])\{V_f\}}{\{U_f^T\}(2i\omega_f[I] - v_f[C_a])\{V_f\}}\right) \tag{a39}$$

$$M_2 = \text{Re}\left(\frac{\{U_f^T\}\{f(F_f)\}}{4\{U_f^T\}(2i\omega_f[I] - v_f[C_a])\{V_f\}}\right) \tag{b39}$$

$$N_1 = \text{Im}\left(\frac{\{U_f^T\}(i\omega_f[C_a] + 2v_f[K_a])\{V_f\}}{\{U_f^T\}(2i\omega_f[I] - v_f[C_a])\{V_f\}}\right) \tag{c39}$$

$$N_2 = \text{Im}\left(\frac{\{U_f^T\}\{f(F_f)\}}{4\{U_f^T\}(2i\omega_f[I] - v_f[C_a])\{V_f\}}\right) \tag{d39}$$

Demanding steady state yields:

$$D_1 P = 0 \rightarrow = P(M_1 v_\delta + M_2 P^2) = 0 \rightarrow P = \begin{cases} 0 \\ \sqrt{\dfrac{M_1 v_\delta}{M_2}} \end{cases} \tag{40}$$

The results of the MS analysis and a comparison to the numerical results are presented in figure 11, showing good coherence with the numerical ones, but give an overshoot in the first mode and lower values in the second. Since the multiple scales is derived at the proximity of the flutter velocity, it is only valid at this region, and the higher stability thresholds are not obtained with it.
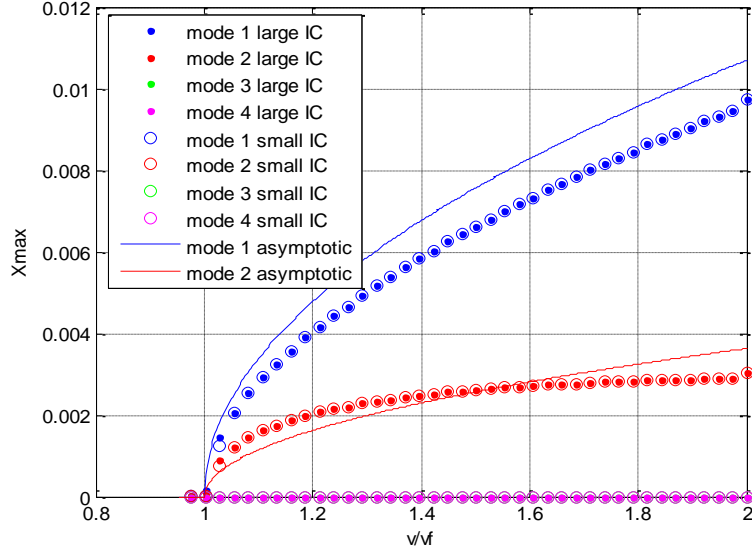

Figure 11: asymptotic solution and comparison to numerical results

VI. Parametric study

The effects of two parameters were examined in the parametric study:

- The effect of the preload.
- The effect of the non-linearity-parameter λ

A. Preload

A plot presenting the flutter/divergence onset, and the second bifurcation point, is presented in Fig. 12. The second bifurcation point is the upper limit of the validity of the analysis model, since above this threshold the oscillation is in multiple frequencies. From the experimental point of view, above these speeds the oscillations lost orbital stability. This makes this threshold a limit on energy harvesting, since energy harvesting from a non-periodic oscillation is more difficult, and probably less efficient. Figure 11 shows that as the preload is increased, the region of periodic oscillations decreases. Higher preload means smaller working region for energy harvesting.

A plot of the average power at different velocities for different values of preload is presented in Fig. 13. The plot shows that the input energy increases with airspeed for all preload values. A steep increase in the slope occurs at the second stability threshold. Above this threshold the energy increases, however, it would be difficult to harvest.

An optimal pretension cannot be determined for the whole airspeed range. A specific pretension would have to be determined based on the target airspeed range.

B. Divergence before flutter

Figure 12 shows that for high values of preload linear flutter analysis predicts divergence before flutter. In the non-linear analysis, as in the experiment, there is no static divergence, and the membrane always flutters. This is due to the nonlinear stiffening.

The effect of the nonlinear stiffening on divergence can be explained using a simplified, static 2D model shown in Fig. 14. A plate is mounted on a nonlinear spring having linear and cubic components. Moment equilibrium on the plate yields:
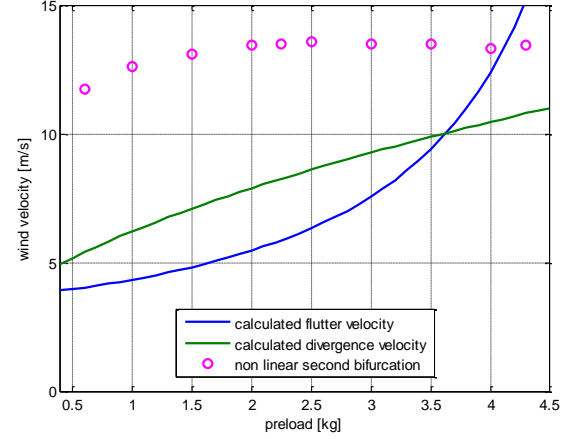

Figure 12: Flutter, divergence, and second bifurcation onset velocities as a function of preload
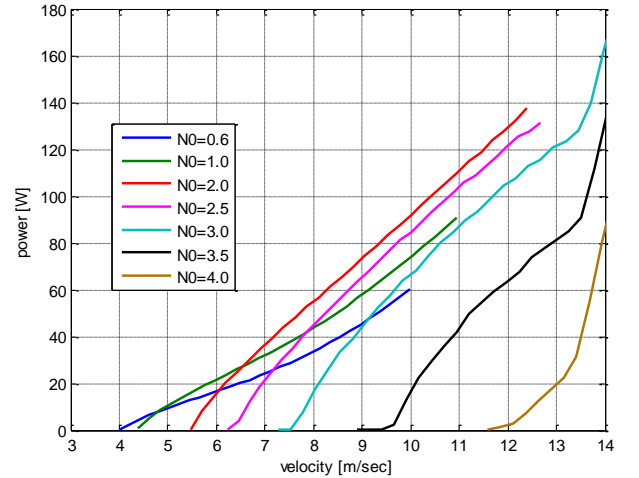
Figure 13: Average input power as a function of airspeed, for different values of preload (kg)
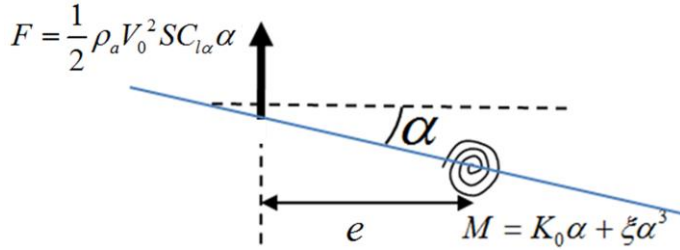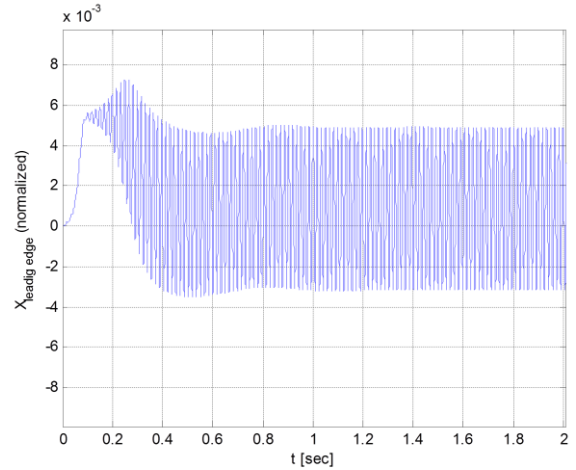
$$\rho V_0^2 S C_{L\alpha} e\alpha / 2 = K_0\alpha + \xi\alpha^3 \tag{30}$$

The non-trivial solution of the equation is:

$$\alpha = \pm\sqrt{\left(\rho V_0^2 S e C_{L\alpha} - 2K_0\right)/2\xi} \tag{31}$$

17

$$F = \frac{1}{2}\rho_a V_0^2 S C_{l\alpha} \alpha$$

$$M = K_0\alpha + \xi\alpha^3$$

Figure 14: 2d strip on a nonlinear spring model

Figure 15: Time history of the oscillation onset
preload=4.3kg, velocity=12.5m/sec

As long as the nominator is negative only the trivial solution exists. As the nominator becomes positive, a new stable solution is created. This is the static divergence. Unlike in the linear case, the deflection in this "divergence" is finite. As a result of the static deflection the stifness is increased, thus increasing the frequencies of the structure, and the flutter velocity. Figure 14 shows a time history of the onset of the oscillation with 4.3 kg preload and airspeed above divergence velocity and below flutter. The displacement starts as non oscillating divergence (0<t<0.1), which then turns into LCO. A few limitations on the discussion above arenoted: The oscillations shown in Fig. 14 start at zero frequency and develop into LCO of a certain frequency. The aerodynamic model used to compute this response assumes a single frequency (in this case, the LCO frequency was used). Therefore, the result shown in Fig. 15 is not accurate, but rather serves to demonstrate the mechanism of the phenomenon of LCO at divergence speed. For the same reason, it is very difficult to accurately predict the onset of flutter in the "divergence before flutter" preload regions with the aerodynamic model used in this study.

C. Non linearity parameter λ

The nonlinearity parameter λ is defined in Eq. (A2). It multiplies all of the nonlinear terms in the membrane's equation of motion (A2). The λ parameter represents the magnitude of the nonlinear stiffness terms, and is linearly dependent on the modulus of elasticity. Figures 16 and 17 show the power and vibration-amplitude at different airspeeds for different λ values. The oscillation frequency is independent of λ. The relation between the amplitude and λ and between the power and λ is given in Eq. 32.
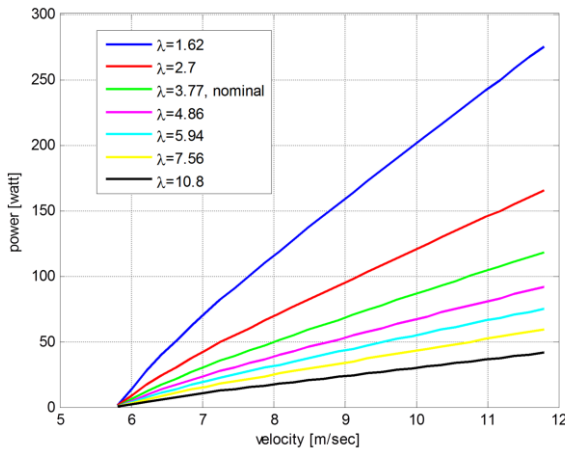

Figure 16: Variation of average power with airspeed for different values of λ, *preload of 2.5 Kg*
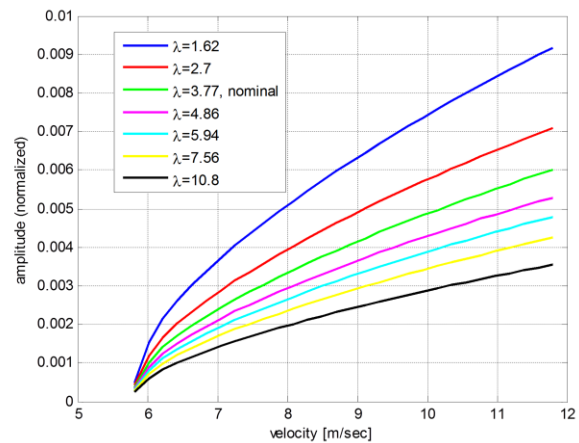

Figure 17: Variation of oscillation amplitude with airspeed for different values of λ, *preload of 2.5 Kg*

18

$$Amplitude \propto \frac{1}{\sqrt{\lambda}}; \qquad P \propto \frac{1}{\lambda}$$

<div align="right">(32)</div>

It is noted that although λ is dependent on the modulus of elasticity, changing the modulus of elasticity has a wider effect on the problem due to its effect on the shear modulus, and thus on the torsion frequencies and flutter velocity.

VII.   Experimental study

A. Setup

To verify the computational model a series of wind tunnel tests was conducted, in which a 0.025 by 0.6 m Mylar membrane was clamped to the tunnel ceiling and pre-loaded by various weights, ranging from 0.5 to 4.5 kg. Figure 18 shows a schematic sketch and a photo of the test setup. By gradually increasing the flow speed divergence and flutter speeds were measured for each loading case. At speeds above flutter speed the frequency and amplitude of the membrane vibrations were recorded.

The measurement setup consists of two strain gauges, an accelerometer, a stroboscope, and a simple camera. The airspeed is measured by the internal wind speed gauges that are part of the wind tunnel. All of the measurement devices except for the stroboscope are connected to the wind-tunnel data acquisition system, and are thus synchronized. The two unidirectional longitudinal strain gauges are mounted on two opposite sides of the membrane middle axis. The gauges are located ~50mm above the bottom clamping device (the exact distance depends on the pretension). These gauges are used for two purposes: Measure the oscillation's amplitude and frequency, and provided online measurement of the pre-tension. The latter is highly important since the preload is somewhat reduced during the experiment- First due to the clamping, and then during the oscillations. The accelerometer

Figure 18: test setup, *left: schematic sketch, right: photo*

is attached to the lower clamping device, close to the base of the membrane. Though the clamping device is relatively rigid in comparison with the membrane, the membrane-induced oscillations were large enough to yield sufficient readings for spectral analysis. In addition to the strain gauges and the accelerometer, in certain parts of the experiment a stroboscope was used to visualize the oscillation's mode shape. This was done by setting the scope to a frequency that is close to the flutter frequency. Since the stroboscope operates in a single frequency, when the oscillation is harmonic (or relatively close to harmonic), a clean mode shape is seen. When the oscillation is non-harmonic the picture obtained by the stroboscope is smeared, giving a good indication on the loss of orbital stability.

The experiments took place in the Faculty of Aerospace Engineering's subsonic wind tunnel. The wind tunnel has an open stream circulation. It allows work at wind speeds in the range of 0 to 90 m/sec. The inlet has an area ratio of 1:25. Eight nets are installed in it in order to reduce turbulence and the effect of outside wind gusts. The experiment cell is built from four frames that, together, create a square section with height and width of one meter and length of three meters. The wind tunnel enables Reynolds numbers of up to six million, and low turbulence level of less than half percent. The stagnation pressure is atmospheric pressure, and the air temperature is the same as the outside temperature.
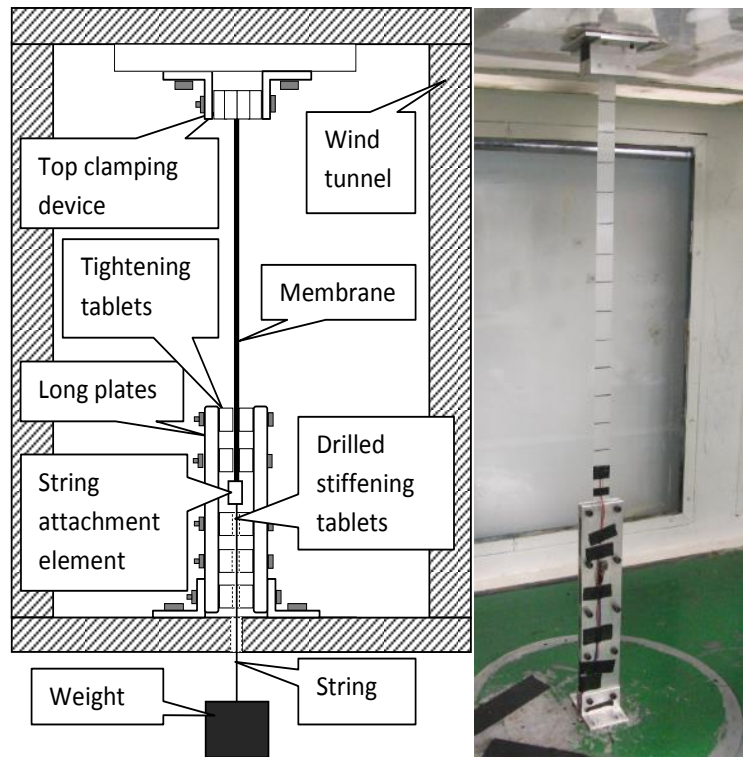
B. Test Procedure and Results

The test was performed with various preloading weights, ranging from 0.5 to 4.5 kg. The test procedure for each loading case was as follows: First the bottom side of the membrane was unrestrained, allowing it to lengthen freely. Then a weight was suspended on the membrane bottom end, and a measurement of the strain was taken. The bottom clamping device was tightened on the membrane and another strain measurement was taken. The airspeed in the tunnel was gradually raised until flutter onset. After the flutter velocity was established, the speed was slightly decreased and an airspeed sweep through the flutter velocity was recorded. The oscillations at various wind velocities above flutter were then recorded, in increments of ~0.5m/s. The length of each recording time window was about three seconds. The velocities were raised until loss of orbital stability. Finally, the airspeed was gradually lowered to zero while recording the oscillations.

Figure 19 shows the preload as measured on the free (unclamped) membrane and on the clamped membrane, before and after each test, showing that the preload was reduced due to the clamping and also during the oscillations. For comparison with results from numerical analysis, the value of the clamped load before test was used.

Figure 19: Measured vs. actual preload at different stages of each experiment

Figure 20 shows a comparison of the flutter (and divergence) velocities and frequencies for each loading case, as computed numerically and measured in the wind tunnel. The flutter frequencies are in good agreement with the numerical results. The flutter speed is in good agreement up to preload of ~3.5, where the analysis yields divergence before flutter. In the experiment there is no divergence, but the LCO onset velocities in this airspeed range correspond to the computed divergence velocities, as discussed in section V.A.
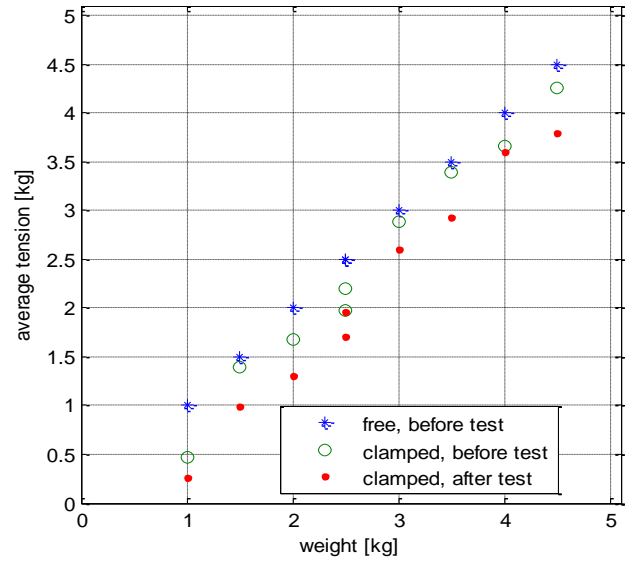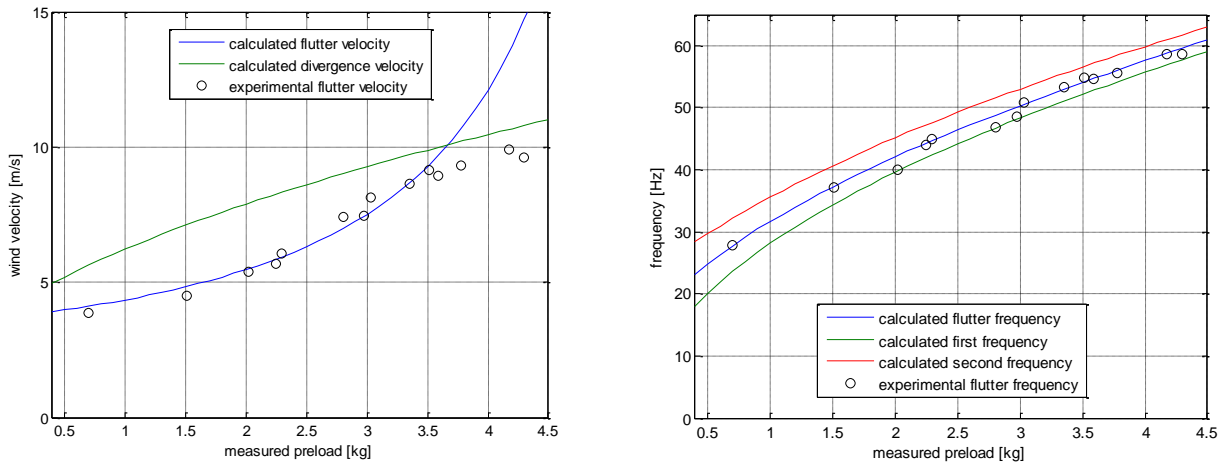

Figure 20: Flutter velocities (left) and frequencies (right) as a function of preload – Comparison of experimental and numerical results

Figure 21 shows the change in LCO frequency with increased airspeed, for different values of preload, as obtained in the experiment and in the analysis. The resolution of the numerical results is 0.61 Hz. The numerical results are in good agreement with the experiment. The loss of orbital stability in the experiment, in the low pretension values, occurred in a lower speed than that predicted in the analysis (not shown).

Figure 22 shows a comparison of sample time history plot of the strains from the analysis and the experiment. The plot is taken from the results with 2.25 kg preload at airspeed of 8.1m/s. A slight static offset appears between the two sets of results. This offset probably results from the preload reduction during the oscillation that was presented in Fig. 19. Otherwise, the results are in good agreement. Both plots show an oscillation in two frequencies, the higher of which is dominant, as discussed in section III.E. and shown in section IV.B., Fig. 10. The plot also shows good correspondence between calculated amplitude and the amplitude recorded in the experiment.
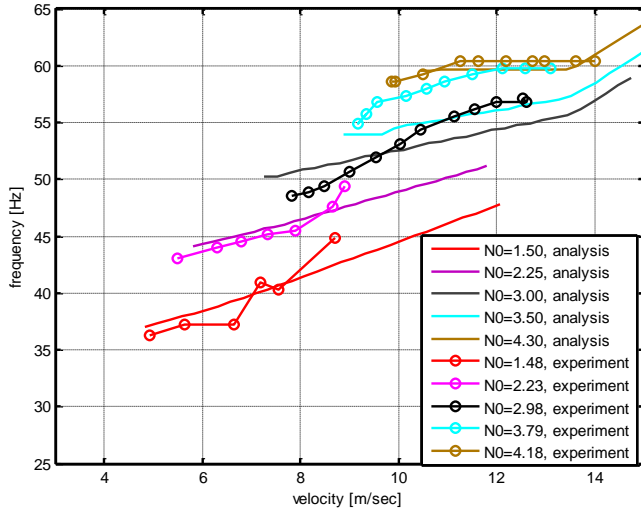

Figure 21: Variation of LCO frequency with airspeed for different preload values: Analysis Vs. experiment
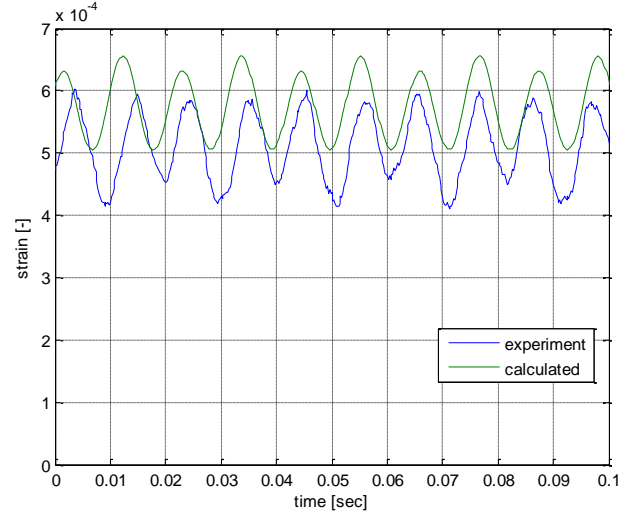

Figure 22: Time history comparison of strains, *pretension=2.25 kg, air velocity=8.1 m/sec*

VIII.   Summary and Conclusions

The paper presented a numerical, analytical and experimental study of the phenomenon of LCO in a pre-tensed membrane strip, for the purpose of energy harvesting. The mathematical model used in the numerical analysis was of a pre-tensed beam, with nonlinear, coupled bending and torsional stiffening due to large deformation. The aerodynamic model was a potential strip theory model. The experimental study was based on a series of wind tunnel tests, in which the flutter onset velocity was detected, and the post-flutter LCO oscillations were recorded via strain gauge readings. The numerical results were in good agreement with the analytical calculation in terms of flutter velocity and amplitudes in the stable-oscillation region. The numerical results were in good agreement with the experimental results, in terms of flutter velocity and oscillation frequencies, for most preload regions. In the region of high preload the linear stability analysis predicts divergence before flutter. In the experiment, and in the nonlinear analysis, LCO occurred at the (linearly predicted) divergence speed. This was explained to be a result of the nonlinear stiffening, due to large deformations.

From an energy harvesting point of view, the study showed that for every airspeed, the optimal preload, which is the preload that yields maximum power, is different. It was also shown that for each preload value there is a working region of airspeeds suitable for energy harvesting. This region is bounded from below by the flutter velocity and from above by the second stability threshold, after which the oscillations lose their orbital stability and become non-periodic. This working region becomes smaller with higher preload.

Further research is recommended in which the energy harvesting system is taken into account and coupled with the aeroelastic equation. The current study doesn't accurately predict the LCO beyond the loss of orbital stability and the onset of LCO at the divergence velocities. This could be improved by use of time domain, instead of frequency domain, aerodynamics.

21

IX.   References

1. Ward, L., and Freyne, S., "Windbelt, Cheap Generator Alternative, Set to Power Third World," June 2007, http://www.popularmechanics.com/science/energy/solarwind/4224763?series=37an.

2. Sundararajan, V., Romero, E., Bonilla, N., and Martinez, C., "Energy Harvesting from Fluttering Membranes," 10th Latin American and Caribbean Conference for Engineering and Technology, Panama City, Panama, July 2012, pp. 1–6.

3. Smith, R. W. and Shyy, W., "Computational Model of Flexible Membrane Wings in Steady Laminar Flow," AIAA Journal, Vol. 33, No. 10, 1995, pp. 1769–1777.

4. Smith, R. W. and Shyy, W., "Computation of Unsteady Laminar Flow over a Flexible Two-Dimensional Membrane Wing," Physics of Fluids, Vol. 7, No. 9, 1995, pp. 2175–2184.

5. Lian, Y., Shyy, W., Viieru, D., and Zhang, B., "Membrane Wing Aerodynamics for Micro Air Vehicles," Progress in Aerospace Sciences, Vol. 39, 2003, pp. 425–465.

6. Scott, R. C., Bartels, R. E., and Kandil, O. A., "An Aeroelastic Analysis of a Thin Flexible Membrane," 48th AIAA/ASME/ASCE/AHS/ASC Structures, Structural Dynamics, and Materials Conference, AIAA, Honolulu, Hawaii, 2007, pp. 7459–7475, AIAA-2007-2316.

7. Gordnier, R. E., "High-Fidelity Computational Simulation of a Membrane Wing Airfoil," Journal of Fluids and Structures, Vol. 25, 2009, pp. 897–917.

8. Rojratsirikul, P., Wang, Z., and Gursul, I., "Unsteady Fluid-Structure Interactions of Membrane Airfoils at Low Reynolds Numbers," Experiments in Fluids, Vol. 46, 2009, pp. 859–872.

9. Tiomkin, S., Raveh, D. E., and Arieli, R., "Parametric Study of a Two Dimensional Membrane Wing in Viscous Laminar Flow," 29th AIAA Applied Aerodynamics Conference, AIAA, Honolulu, Hawaii, 2011, AIAA-2011-3023.

10. Dowell, E. H., "Panel Flutter: A Review of the Aeroelastic Stability of Plates and Shells," AIAA Journal, Vol. 8, No. 3, 1970, pp. 385–399.

11. Levin, D., and Karpel, M., "Limit Cycle Oscillations of Plate-Type Fins Using Increased-Order Models," Journal of Aircraft, Vol. 48, No. 2, 2011, pp.715-719

12. Wang, I., and Dowell, E. H., "Flutter of Rectangular Plates in Three Dimensional Incompressible Flow with Various Boundary Conditions: Theory and Experiment," ASME International Design Engineering Technical Conferences & Computers and Engineering Conference, ASME, Chicago, IL, 2012, pp. 1–13.

13. Dowell, E. H., "Nonlinear Oscillations of a Fluttering Plate. II," AIAA Journal, Vol. 5, No. 10, 1967, pp. 1856-1862

14. Kuo, C. C., Morino, L., and Dugundji, J., "Perturbation and Harmonic Balance Methods for Nonlinear Panel Flutter," AIAA Journal, Vol. 10, No. 11, 1972, pp. 1479-1484

15. Patil, M. J., and Hodges, D. H., "Limit Cycle Oscillations in High-Aspect-Ratio Wings," Journal of Fluids and Structures, Vol. 15, 2001, pp. 107–132

16.Tang, D. M., and Dowel, E. H., "Effects of Geometric Structural Nonlinearity on Flutter and Limit Cycle Oscillations of High-aspect-ratio Wings," Journal of Fluids and Structures, Vol. 19, 2004, pp. 291–306.

17. L. Meirovitch, Methods of Analytical Dynamics, McGraw-Hill Book Company, New York (Sixteenth Printing, 1993), Dover Publications, Mineola, NY, 2003.

18. Wright,J. R., and Cooper,J. E., "Introduction to Aircraft Aeroelasticity and Loads," American Institute of Aeronautics and Astronautics, 2007.

19. ZONA Technologies, ZAERO Theoretical Manual, Version 8.5, ZONA Technologies, 2011.

Appendix A. Mode Shapes and Coefficients of the Final Aeroelastic Equation

Mode Shapes and frequencies:

$$W_1(x) = \sin\left(\frac{\pi x}{a}\right); \qquad \theta_1(x) = 0; \qquad \omega_1 = \frac{\pi}{a}\sqrt{\frac{\sigma_0}{\rho}}$$

$$W_2(x) = 0; \qquad \theta_2(x) = \sin\left(\frac{\pi x}{a}\right); \qquad \omega_2 = \frac{\pi}{a}\sqrt{\frac{\sigma_0 + \dfrac{GJ}{I_p}}{\rho}}$$

$$W_3(x) = \sin\left(\frac{2\pi x}{a}\right); \qquad \theta_3(x) = 0; \qquad \omega_3 = \frac{2\pi}{a}\sqrt{\frac{\sigma_0}{\rho}}$$

$$W_4(x) = 0; \qquad \theta_4(x) = \sin\left(\frac{2\pi x}{a}\right); \qquad \omega_4 = \frac{2\pi}{a}\sqrt{\frac{\sigma_0 + \dfrac{GJ}{I_p}}{\rho}} \tag{A1}$$

Coefficients of the final aeroelastic equation:

$$K_{a11} = K_{a33} = -\frac{\rho_a L_z(k)}{\rho A}; \qquad K_{a12} = K_{a34} = \frac{b\rho_a L_\alpha(k)}{2\rho A}$$

$$K_{a21} = K_{a43} = \frac{-b\rho_a M_z(k)}{2\rho I_p}; \qquad K_{a22} = K_{a44} = \frac{b^2 \rho_a M_\alpha(k)}{4\rho I_p}$$

$$C_{a11} = C_{a33} = -\frac{b\rho_a L_{\dot{z}}(k)}{2\rho A}; \qquad C_{a12} = C_{a34} = \frac{b^2 \rho_a L_{\dot{\alpha}}(k)}{4\rho A}$$

$$C_{a21} = C_{a43} = -\frac{b^2 \rho_a M_{\dot{z}}(k)}{4\rho I_p} \qquad C_{a22} = C_{a44} = \frac{b^3 \rho_a M_{\dot{\alpha}}(k)}{8\rho I_p}$$

$$K_1 = \omega_1^2; \qquad K_2 = \omega_2^2; \qquad K_3 = 4\omega_1^2; \qquad K_4 = 4\omega_2^2$$

$$\xi_{11} = \frac{1}{4}\lambda; \qquad \xi_{12} = \frac{b^2\lambda}{16}; \qquad \xi_{13} = \lambda; \qquad \xi_{14} = \frac{b^2}{12}\lambda; \qquad \xi_{234} = \frac{b^2\lambda}{6};$$

$$\xi_{21} = \frac{3\lambda}{4}; \qquad \xi_{22} = \frac{3b^2\lambda}{80}; \qquad \xi_{23} = \lambda; \qquad \xi_{24} = \frac{3b^2\lambda}{20}; \qquad \xi_{134} = 2\lambda;$$

$$\xi_{31} = \lambda; \qquad \xi_{32} = \frac{b^2}{12}\lambda; \qquad \xi_{33} = 4\lambda; \qquad \xi_{34} = b^2\lambda; \qquad \xi_{124} = \frac{b^2}{6}\lambda;$$

$$\xi_{41} = 1\lambda; \qquad \xi_{42} = \frac{3b^2\lambda}{20}; \qquad \xi_{43} = 12\lambda; \qquad \xi_{44} = \frac{3b^2\lambda}{5}; \qquad \xi_{123} = 2\lambda;$$

$$C_1 = 2\zeta_1\omega_1; \qquad C_2 = 2\zeta_2\omega_2; \qquad C_3 = 2\zeta_3\omega_3; \qquad C_4 = 2\zeta_4\omega_4$$

$$\lambda \equiv \frac{E\pi^4}{\rho a^4}; \qquad \omega_1 \equiv \frac{\pi}{a}\sqrt{\frac{\sigma_0}{\rho}}; \qquad \omega_2 \equiv \frac{\pi}{a}\sqrt{\frac{\sigma_0 + GJ/I_p}{\rho}} \tag{A2}$$

Appendix B: The V-g method (fit to the non-dimensional formulation)

The dynamic equation that represents the linearized aeroelastic system can be written by:

$$[A]\{\ddot{X}\} + ([D] - v[B])\{\dot{X}\} + ([E] - v^2[C])\{X\} = 0 \tag{B1}$$

where:

A is the inertial matrix (in our case a unity matrix)

B is the aerodynamic damping matrix (scaled by ρv)

C is the aerodynamic stiffness matrix (scaled by ρv^2)

D is the structural damping matrix

E is the structural stiffness matrix

The solution is based on adding a fictitious damping into the system in the form of a complex stiffness matrix multiplier i*g.

$$[A]\{\ddot{X}\} + ([D] - v[B])\{\dot{X}\} + \left((1 + ig)[E] - v^2[C]\right)\{X\} = 0 \tag{B2}$$

Neglecting the structural damping, assuming a harmonic solution (2.3), dividing by -w^2, and extracting the (non-dimensional) velocity from the definition of non-dimensional frequency (2.4) yields an eigenvalue problem (C5).

$$\{X\} = \{X_0\}e^{i\omega t}; \qquad \{\dot{X}\} = i\omega\{q_0\}e^{i\omega t}; \qquad \{\ddot{X}\} = -\omega^2\{q_0\}e^{i\omega t} \tag{B3}$$

$$k = \frac{\omega b}{v} \rightarrow v = \frac{\omega b}{k} \tag{B4}$$

$$\left(\underbrace{[A] + i\left(\frac{b}{k}\right)[B] + \left(\frac{b}{k}\right)^2[C]}_{F} - \underbrace{\frac{1+ig}{w^2}}_{\lambda}[E]\right)\{X_0\} = \{0\} \tag{B5}$$

Note that the solution is a function of the non-dimensional frequency and velocity k and v.

The next step in the solution is assuming a value of k and solving the eigenvalue problem C6

$$([F] - \lambda[E])\{X_0\} = \{0\} \tag{B6}$$

From each eigenvalue we derive a frequency, a damping multiplier and a velocity using C7, C8

$$\lambda_m = \frac{1}{\omega_m^2} + i\frac{g}{\omega_m^2} \tag{B6}$$

$$\omega_m = \frac{1}{\sqrt{\mathrm{Re}(\lambda_m)}}; \qquad g_m = \frac{\mathrm{Im}(\lambda_m)}{\mathrm{Re}(\lambda_m)}; \qquad v_m = \frac{\omega_m b}{k} \tag{B7}$$

The results are plotted on two graphs of (w V.S. v, aka v-w plot) and (g V.S v, aka v-g plot).

The procedure is repeated for a multitude of k's each time adding the results to the graph. Note that for each assumed k, the aerodynamic coefficients are recalculated. The result is a full v-g and v-w plot.

When the v-g plot crosses reaches zero, it means that no damping should be subtracted from the system in order for it to lose stability. That is the flutter speed. The fluttering frequency and modes are obtained from the v-w plot at the flutter velocity.

Structural damping can be taken into account by offsetting the vg plot by $\zeta/2$ (ζ is the damping ratio).

The damping and frequencies obtained from the v-g plot are only correct at flutter speed. In the rest of the region, the solution is wrong due to the added damping and due to the fact that the solution assumes oscillation in a single frequency. This assumption is only reasonable when the structure loses stability and one frequency becomes strongly dominant.

Static instability (divergence) can also be seen. It is identified by a frequency that reaches zero.